

# Calcium buffers and L-type calcium channels as modulators of cardiac subcellular alternans

Yi Ming Lai<sup>1,\*</sup>, Stephen Coombes, Rüdiger Thul

*Centre for Mathematical Medicine and Biology, School of Mathematical Sciences,  
University of Nottingham, Nottingham, NG7 2RD, UK*

---

## Abstract

In cardiac myocytes, calcium cycling links the dynamics of the membrane potential to the activation of the contractile filaments. Perturbations of the calcium signalling toolkit have been demonstrated to disrupt this connection and lead to numerous pathologies including cardiac alternans. This rhythm disturbance is characterised by alternations in the membrane potential and the intracellular calcium concentration, which in turn can lead to sudden cardiac death. In the present computational study, we make further inroads into understanding this severe condition by investigating the impact of calcium buffers and L-type calcium channels on the formation of subcellular calcium alternans when calcium diffusion in the sarcoplasmic reticulum is strong. Through numerical simulations of a two dimensional network of calcium release units, we show that increasing calcium entry is proarrhythmogenic and that this is modulated by the calcium-dependent inactivation of the L-type calcium channel. We also find that while calcium buffers can exert a stabilising force and abolish subcellular  $\text{Ca}^{2+}$  alternans, they can significantly shape the spatial patterning of subcellular calcium alternans. Taken together, our results demonstrate that subcellular calcium alternans can emerge via various routes and that calcium diffusion in the sarcoplasmic reticulum critically determines their spatial patterns.

*Keywords:* calcium cycling, synchrony, luminal diffusion, subcellular calcium

---

\*Corresponding author

<sup>1</sup>yi.lai1@nottingham.ac.uk

alternans, saddle-node bifurcation

---

## 1. Introduction

Cardiac arrhythmias constitute a leading public health problem and cause most cases of sudden cardiac death. In the US alone, sudden cardiac death accounts for approximately 300,000 – 450,000 lives every year [1]. Among the many forms of cardiac arrhythmias, cardiac alternans feature prominently. This rhythm disturbance at the level of a single cardiac myocyte is characterised by alternating patterns of the membrane potential and the intracellular calcium ( $\text{Ca}^{2+}$ ) concentration on successive beats. For instance, at one beat, a long action potential duration (APD) is accompanied by a large intracellular  $\text{Ca}^{2+}$  transient, while on the next beat, the APD is shortened concomitant with a small amplitude  $\text{Ca}^{2+}$  transient. As a consequence, contractile efficiency is impaired, which in turn can cause a detrimental reduction in blood flow. In early experimental studies, the intracellular  $\text{Ca}^{2+}$  concentration was averaged across a cardiac myocyte. The advent of high-resolution microscopy revealed that alternating  $\text{Ca}^{2+}$  dynamics were already present at individual  $\text{Ca}^{2+}$  release units (CRU). While one CRU follows a pattern of large-small-large  $\text{Ca}^{2+}$  transients, neighbouring CRUs exhibit small-large-small  $\text{Ca}^{2+}$  transients. Crucially, both CRUs experience the same membrane potential. These findings gave rise to the concept of subcellular  $\text{Ca}^{2+}$  alternans [2–10] and illustrated that nonlinear processes govern cardiac dynamics across multiple scales: the cell wide membrane potential and the  $\text{Ca}^{2+}$  fluxes restricted to single dyadic clefts.

The existence of subcellular  $\text{Ca}^{2+}$  alternans reinforces the notion of cardiac myocytes as a network of networks. Each CRU can be conceptualised as a network of interacting components such as L-type  $\text{Ca}^{2+}$  channels, sodium-calcium exchangers (NCXs) and ryanodine receptors (RyRs). These local networks are then coupled via  $\text{Ca}^{2+}$  diffusion through both the cytosol and the sarcoplasmic reticulum (SR). This interconnectedness offers multiple explanations for the origin of subcellular  $\text{Ca}^{2+}$  alternans. On the one hand, we have previously shown

that  $\text{Ca}^{2+}$  alternans can emerge purely through coupling [11]. In other words,  
30 an isolated CRU displays a regular period-1 orbit, but upon increasing the coupling strength between CRUs, period-2 orbits characteristic of  $\text{Ca}^{2+}$  alternans emerge. Crucially, the shape of the  $\text{Ca}^{2+}$  alternans may depend on the form of coupling. In a recent model of  $\text{Ca}^{2+}$  cycling,  $\text{Ca}^{2+}$  alternans emerge for dominant cytosolic coupling via the traditional period-doubling bifurcation, where  
35 an eigenvalue of the associated linearised map exits the unit disk through  $-1$  along the real axis [12, 13]. Here, each node exhibits alternating  $\text{Ca}^{2+}$  dynamics, and neighbouring nodes (or nodes in different parts of a cell) oscillate out-of-phase with each other. For dominant luminal coupling, there is a saddle-node bifurcation, where the leading eigenvalue leaves the unit disk at  $+1$  along the  
40 real axis. In this case, each node follows a period-1 orbit, but the amplitudes of neighbouring CRUs varies. On the other hand, changes to the molecular components of a CRU can induce  $\text{Ca}^{2+}$  alternans, exemplified by weakening sarco-endoplasmic  $\text{Ca}^{2+}$  ATP (SERCA) pumps or increasing  $\text{Ca}^{2+}$  flux through L-type  $\text{Ca}^{2+}$  channels.

45 To date, investigations on how  $\text{Ca}^{2+}$  alternans emerge due to modifications at the CRU level have almost exclusively focussed on dominant cytosolic coupling [3, 14–20]. However, the question as to whether  $\text{Ca}^{2+}$  diffusion in the SR is slow or fast — and hence weak or strong — is still unanswered [21–23]. Here, we focus on strong SR  $\text{Ca}^{2+}$  diffusion and explore the impact of two modifiers  
50 of the local  $\text{Ca}^{2+}$  dynamics on the genesis of subcellular  $\text{Ca}^{2+}$  alternans: L-type  $\text{Ca}^{2+}$  channels and  $\text{Ca}^{2+}$  buffers.

The L-type  $\text{Ca}^{2+}$  channel has received significant attention due to its central role in excitation-contraction coupling [24–26]. Its contribution to the formation of  $\text{Ca}^{2+}$  alternans is ambiguous though [27]. On the one hand, several studies  
55 have provided compelling evidence that altering the dynamics of L-type  $\text{Ca}^{2+}$  channel through e.g. cooperative gating or reducing the current can either promote or inhibit  $\text{Ca}^{2+}$  alternans [28, 29]. On the other hand,  $\text{Ca}^{2+}$  alternans have been observed with clamped membrane voltage, thus limiting the degree of control that L-type  $\text{Ca}^{2+}$  channels can exert on the genesis of  $\text{Ca}^{2+}$  alternans

[30]. Here, we investigate the role of  $\text{Ca}^{2+}$ -dependent inactivation of the L-type  $\text{Ca}^{2+}$  channel on the dynamics of a CRU, which occurs in addition to voltage-dependent activation and inactivation. [31, 32]. We find that  $\text{Ca}^{2+}$ -dependent inactivation affects the formation of subcellular  $\text{Ca}^{2+}$  alternans in a nontrivial manner that depends on the unitary current of the L-type  $\text{Ca}^{2+}$  channel.

$\text{Ca}^{2+}$  buffers are essential for cardiac function, not least because activation of the cytoplasmic buffer troponin C determines how strongly a cardiac myocyte contracts [24]. In addition, the buffers calsequestrin and calmodulin have been shown to vitally shape the dynamics of cardiac myocyte including an impact on the refractoriness of RyRs [33–47]. As has been demonstrated both experimentally and theoretically for numerous cell types and  $\text{Ca}^{2+}$  releasing channels, including the inositol-1,4,5-trisphosphate receptor,  $\text{Ca}^{2+}$  buffers can fundamentally alter the dynamics of intracellular  $\text{Ca}^{2+}$  dynamics ranging from local  $\text{Ca}^{2+}$  release events such as  $\text{Ca}^{2+}$  sparks and  $\text{Ca}^{2+}$  puffs to global  $\text{Ca}^{2+}$  patterns such as travelling  $\text{Ca}^{2+}$  waves. Due to the nonlinear dynamics of  $\text{Ca}^{2+}$  buffers, direct predictions are difficult to make. We show through numerical simulations that  $\text{Ca}^{2+}$  buffers can both promote and inhibit subcellular  $\text{Ca}^{2+}$  alternans, which adds another facet to the already rich repertoire of buffered  $\text{Ca}^{2+}$  dynamics.

## 2. Materials and methods

We consider a two-dimensional network of  $15 \times 10$  CRUs, where the dynamics of a node with label  $\mu$  is governed by the Shiferaw-Karma model [30]

$$\frac{dc_s^\mu}{dt} = \beta(c_s^\mu) \left[ \frac{v_i}{v_s} \left( I_r^\mu - \frac{c_s^\mu - c_i^\mu}{\tau_s} - I_{\text{CaL}}^\mu \right) + I_{\text{NCX}}^\mu \right], \quad (1a)$$

$$\frac{dc_i^\mu}{dt} = \beta(c_i^\mu) \left[ \frac{c_s^\mu - c_i^\mu}{\tau_s} - I_{\text{up}}^\mu \right] + \sum_{\eta \in \mathcal{I}_n} \frac{c_i^\eta - c_i^\mu}{\tau_c}, \quad (1b)$$

$$\frac{dc_j^\mu}{dt} = -I_r^\mu + I_{\text{up}}^\mu + \sum_{\eta \in \mathcal{I}_n} \frac{c_j^\eta - c_j^\mu}{\tau_{\text{sr}}}, \quad (1c)$$

$$\frac{dc_u^\mu}{dt} = \frac{c_j^\mu - c_u^\mu}{\tau_a}, \quad (1d)$$

$$\frac{dI_r^\mu}{dt} = -gI_{\text{CaL}}Q(c_u^\mu) - \frac{I_r^\mu}{\tau_r}. \quad (1e)$$

The  $\text{Ca}^{2+}$  concentrations in the subsarcolemmal space and in the cytosolic bulk are denoted by  $c_s^\mu$  and  $c_i^\mu$ , respectively, while the total  $\text{Ca}^{2+}$  concentration in the SR and the  $\text{Ca}^{2+}$  concentration in the unrecruited SR are given by  $c_j^\mu$  and  $c_u^\mu$ , respectively. The  $\text{Ca}^{2+}$  release current from the unrecruited SR into the subsarcolemmal space is  $I_r^\mu$ , and we refer to the L-type  $\text{Ca}^{2+}$  current, the NCX current and the SERCA uptake current by  $I_{\text{CaL}}^\mu$ ,  $I_{\text{NCX}}^\mu$  and  $I_{\text{up}}^\mu$ , respectively. The model contains four diffusive currents with timescales  $\tau_s$ ,  $\tau_c$ ,  $\tau_{\text{sr}}$  and  $\tau_a$ , describing coupling between the subsarcolemmal space and the cytosolic bulk, through the cytosolic bulk between neighbouring CRUs (indexed by  $\mathcal{I}_n$ ), between the total and unrecruited SR, and through the SR between neighbouring CRUs (indexed by  $\mathcal{I}_n$ ), respectively. In some instances, we report the network coupling strengths as inverse of the timescales, i.e.  $\sigma_x = \tau_x^{-1}$ ,  $x \in \{\text{c}, \text{sr}\}$ . The L-type  $\text{Ca}^{2+}$  current is  $I_{\text{CaL}}^\mu = M i_{\text{Ca}} P_o$ , where  $M$  is the number of L-type  $\text{Ca}^{2+}$  channels per dyadic cleft,  $i_{\text{Ca}}$  is the single channel current and  $P_o = dqf$  is the open probability. Here,  $d$  is the value of the fast voltage-dependent activation gate,  $q$  corresponds to the  $\text{Ca}^{2+}$ -dependent inactivation gate and  $f$  to the voltage-dependent inactivation gate. All gates are described by first order kinetics of the form

$$\frac{dx}{dt} = \frac{x_\infty - x}{\tau_x}, \quad x \in \{d, f, q\}. \quad (2)$$

Of particular interest for the present study is

$$q_\infty = \frac{c_e^\gamma}{c_e^\gamma + c_s^\gamma}, \quad (3)$$

where  $c_e$  sets the  $EC_{50}$  value, i.e. the value of the subsarcolemmal  $\text{Ca}^{2+}$  concentration  $c_s$  at which  $q_\infty$  equals 0.5, and  $\gamma$  controls the sensitivity of  $\text{Ca}^{2+}$ -dependent inactivation. Essentially, the larger  $\gamma$  the more step-like the inactivation around a  $\text{Ca}^{2+}$  concentration of  $c_e$ . Buffering is modelled based on the fast-buffer approximation [48, 49] yielding

$$\frac{1}{\beta(c)} = 1 + \frac{B_{\text{SR}} K_{\text{SR}}}{(c + K_{\text{SR}})^2} + \frac{B_{\text{T}} K_{\text{T}}}{(c + K_{\text{T}})^2} + \frac{B_{\text{cd}} K_{\text{cd}}}{(c + K_{\text{cd}})^2}, \quad (4)$$

where  $B_{\text{SR}}$  denotes the total buffer concentration in the SR and  $K_{\text{SR}}$  the associated dissociation constant. Constants with the subscript T and cd have the

same interpretation, but correspond to troponin C and calmodulin, respectively. For all other details of the model including the functional forms  $i_{Ca}$  and  $I_{NCX}$ , we refer the reader to [30]. A list of all parameter values used in this study is provided in Table 1. All simulations are performed under clamped voltage  
85 conditions, and the we employ no-flux boundary conditions.

### 3. Results

To establish a baseline for our findings, we first investigate the dynamics of the CRU network when buffers are clamped over time. In other words, we set  $\beta(c_s^\mu) \equiv \beta_s = \text{const}$  and  $\beta(c_i^\mu) \equiv \beta_i = \text{const}$  for all  $\mu$ . When cytosolic  
90 coupling is dominant, i.e.  $\tau_c \ll \tau_{sr}$  ( $\sigma_c \gg \sigma_{sr}$ ), synchrony is stable for low pacing frequencies as demonstrated in Fig. 1A. We here show a space-time plot of the *unravalled* CRU network, where we index nodes beginning with 1 in the bottom left corner of the two-dimensional CRU network and move upwards in a row-like manner, i.e. index 16 refers to the most left CRU in the second  
95 row from the bottom. When we decrease  $T_p$ , we observe the emergence of subcellular  $Ca^{2+}$  alternans as depicted in Fig. 1B. Each CRU follows a period-2 orbit, where a small amplitude  $Ca^{2+}$  transient on one beat is followed by a large  $Ca^{2+}$  transient on the next beat. Figures 1C and 1D provide a more detailed view on the emergent spatial pattern, where we plot the peak subsarcolemmal  
100  $Ca^{2+}$  concentration on successive beats. The  $Ca^{2+}$  alternans are arranged in an *inside-out* pattern along the long axis of the network, where CRUs within one row show almost identical behaviour, but peak amplitudes vary along the vertical direction. When  $Ca^{2+}$  transients are large in the centre, they are small towards the top and bottom. On the next beat, this pattern is reversed with  
105 large  $Ca^{2+}$  transients at the top and bottom.

For dominant luminal coupling, where  $\tau_c \gg \tau_{sr}$  ( $\sigma_c \ll \sigma_{sr}$ ), we again find stable synchrony at low pacing frequencies (see Fig. 2A). Indeed, the space-time plot of the subsarcolemmal  $Ca^{2+}$  concentration is identical to the one in Fig. 1A, since when all CRUs exhibit the same behaviour, the coupling terms in

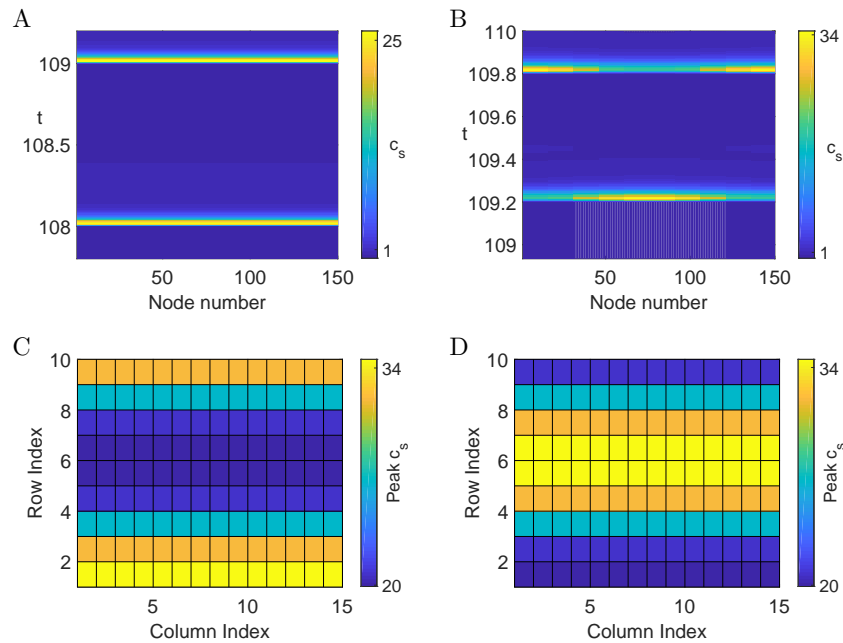


Figure 1: Space-time plot of the subarcolemmal  $\text{Ca}^{2+}$  concentration of the unravelled CRU network for (A)  $T_p = 1\text{s}$  and (B)  $T_p = 0.6\text{s}$ . (C,D) Peak subarcolemmal  $\text{Ca}^{2+}$  concentration on two successive beats across the CRU network. Parameter values as in (B). All other parameter values as in Table 1 and  $\sigma_c = 15\text{s}^{-1}$ ,  $\sigma_{\text{sr}} = 3\text{s}^{-1}$ .

110 Eqs. (1b) and (1c) vanish. The main difference between dominant cytosolic and  
 dominant luminal coupling becomes apparent when we lower  $T_p$ . For the latter,  
 we find subcellular  $\text{Ca}^{2+}$  alternans that emerge via a saddle-node bifurcation at  
 the network level, in contrast to a period doubling bifurcation for the former.  
 As Fig. 2B highlights, each CRU follows a period-1 orbit, but this orbit differs  
 115 amongst the CRUs in the network. Figures 2C and 2D illustrate that here,  
 CRUs on the left form large  $\text{Ca}^{2+}$  amplitude transients, while the transients are  
 smaller towards the right. In the following we will use Figures 2B to 2D as a  
 reference case and contrast them with the network behaviour when we alter the  
 behaviour of the L-type  $\text{Ca}^{2+}$  channel and that of  $\text{Ca}^{2+}$  buffers.

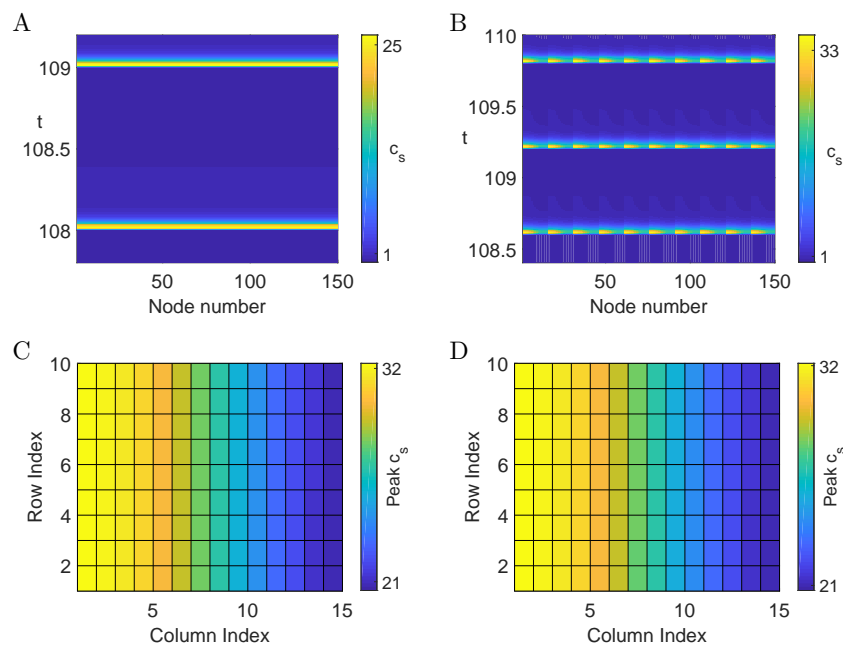


Figure 2: Space-time plot of the subarcolemmal  $\text{Ca}^{2+}$  concentration of the unravelled CRU network for (A)  $T_p = 1\text{s}$  and (B)  $T_p = 0.6\text{s}$ . (C,D) Peak subarcolemmal  $\text{Ca}^{2+}$  concentration on two successive beats across the CRU network. Parameter values as in (B). All other parameter values as in Table 1 and  $\sigma_c = 2\text{s}^{-1}$ ,  $\sigma_{sr} = 15\text{s}^{-1}$ .

### 120 3.1. L-type $\text{Ca}^{2+}$ channel

The extent to which  $\text{Ca}^{2+}$ -dependent inactivation sets in as a function of the subarcolemmal  $\text{Ca}^{2+}$  concentration  $c_s^u$  is controlled by the exponent  $\gamma$  in Eq. (3). When  $\gamma$  is small, the inverse Hill function  $q_\infty$  drops slowly from 1 to 0, while a large value of  $\gamma$  leads to switch-like behaviour around a concentration value of  $c_e$ . As Fig. 3A illustrates, the synchronous network state is stable when  $\gamma$  is small. On the other hand, as  $\gamma$  is increased, subcellular  $\text{Ca}^{2+}$  alternans emerge via a saddle-node bifurcation as shown in Figs. 3B–3D. Figure 3B displays a space-time plot of the unravelled CRU network where the variation of the maxima of the  $\text{Ca}^{2+}$  transients is clearly visible as the colour changes from yellow to blue when we traverse the network. We can also discern changes

125  
130



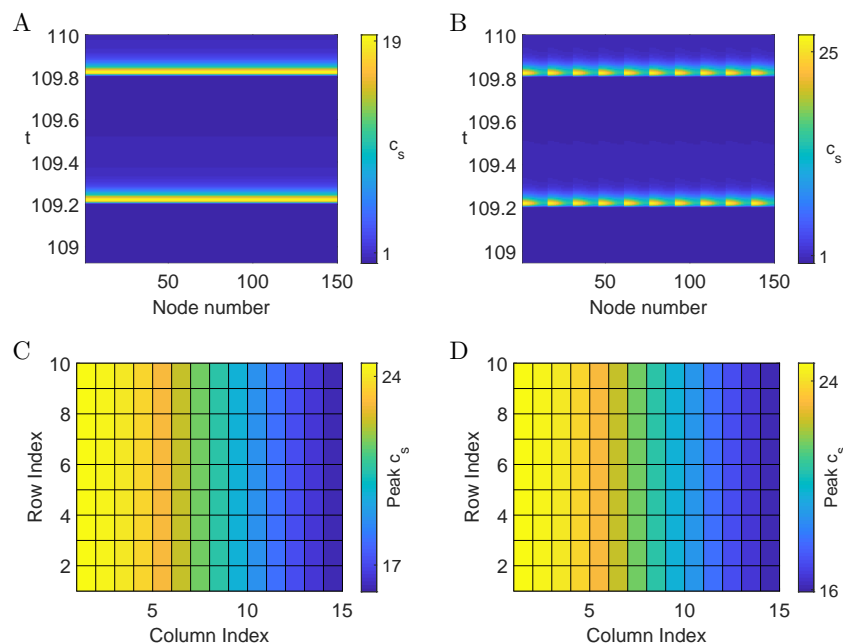


Figure 3: Space-time plot of the subarcolemmal  $\text{Ca}^{2+}$  concentration of the unravelled CRU network for  $i_{\text{Ca}} = 4400 \mu\text{mol C}^{-1} \text{cm}^{-1}$  and (A)  $\gamma = 1$ , (B)  $\gamma = 3$ . (C,D) Peak subarcolemmal  $\text{Ca}^{2+}$  concentration on two successive beats across the CRU network. Parameter values as in (B). For all other parameter values, see Table 1.

in the duration of the  $\text{Ca}^{2+}$  transient as evidenced by the wedge shape of the yellow regions of increased  $\text{Ca}^{2+}$ . Figures 3C and 3D provide more detail on the spatial pattern of the subcellular  $\text{Ca}^{2+}$  alternans. On each beat, large  $\text{Ca}^{2+}$  transients occur towards the left side of the myocyte, while  $\text{Ca}^{2+}$  transients are  
 135 small towards the right side. Note that there is no variation of the  $\text{Ca}^{2+}$  peak amplitudes along the row index. These results suggest that a more gradual  $\text{Ca}^{2+}$ -dependent inhibition of the L-type  $\text{Ca}^{2+}$  channel, i.e. when  $\gamma$  is small, protects cardiac myocytes from subcellular  $\text{Ca}^{2+}$  alternans.

The unitary current of an L-type  $\text{Ca}^{2+}$  channel can be modulated through  
 140 various mechanisms, including  $\beta$ -adrenergic stimulation. The space-time plot in Fig. 4A shows that for small values of  $i_{\text{Ca}}$ , synchrony is stable. However, upon

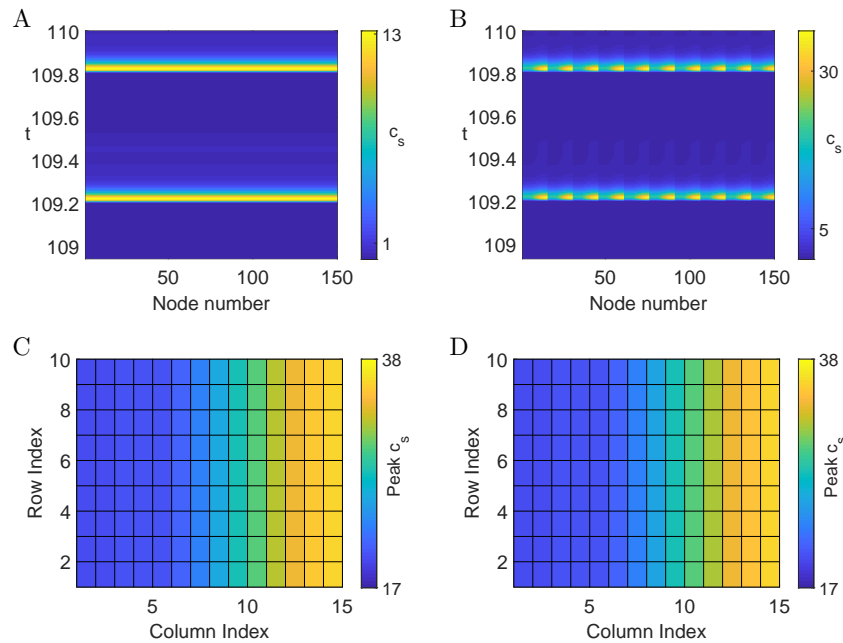


Figure 4: Space-time plot of the subsarcolemmal  $\text{Ca}^{2+}$  concentration of the unravelled CRU network for  $\gamma = 3$  and (A)  $i_{\text{Ca}} = 2200 \mu\text{mol C}^{-1}\text{cm}^{-1}$ , (B)  $i_{\text{Ca}} = 6600 \mu\text{mol C}^{-1}\text{cm}^{-1}$ . (C,D) Peak subsarcolemmal  $\text{Ca}^{2+}$  concentration on two successive beats across the CRU network. Parameter values as in (B). For all other parameter values, see Table 1.

increasing the single channel current, subcellular  $\text{Ca}^{2+}$  alternans emerge via a saddle-node bifurcation. We again observe variations of the  $\text{Ca}^{2+}$  transients in the network similar to those plotted in Fig. 3B. The main difference is the spatial organisation. While the  $\text{Ca}^{2+}$  transients are most pronounced on the left side in Fig. 3, we find here the largest  $\text{Ca}^{2+}$  transients towards the right side. This is already discernible in Fig. 4B, where the tip of the yellow wedges points towards the left (in comparison, the yellow wedges point towards the right in Fig. 3B). A clearer view is provided in Figs. 4C and 4D which show the peak subsarcolemmal  $\text{Ca}^{2+}$  concentration at subsequent beats. The results plotted in Fig. 4 are consistent with experimental findings that upregulation of the L-type  $\text{Ca}^{2+}$  channel is pro-arrhythmogenic [29].

The  $\text{Ca}^{2+}$  profiles depicted in Figs. 3 and 4 suggest that the effect of the unitary L-type  $\text{Ca}^{2+}$  current on the generation of subcellular  $\text{Ca}^{2+}$  alternans depends on the properties of  $\text{Ca}^{2+}$ -dependent inactivation of the channel and vice versa. In Fig. 5 we provide a more comprehensive view on the interplay between these two components. For a given pair of  $\gamma$  and  $i_{\text{Ca}}$ , we compute the maximal difference in peak subsarcolemmal  $\text{Ca}^{2+}$  on successive beats for a CRU with index  $\mu$ , i.e

$$\theta^\mu = \max_i |c_s^{\mu,i} - c_s^{\mu,i+1}|, \quad (5)$$

where  $c_s^{\mu,i}$  is the maximum of  $c_s^\mu$  on the  $i$ th beat. Then, we determine the maximum of all  $\theta^\mu$  across the CRU network,  $\theta = \max_\mu \theta^\mu$ . When  $i_{\text{Ca}}$  is small,  $\theta$

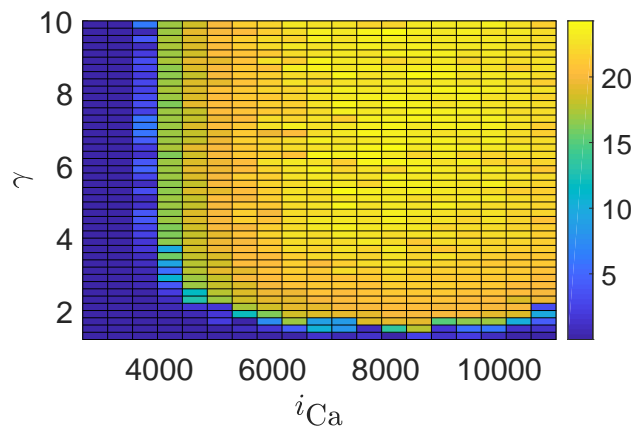


Figure 5: Maximal beat-to-beat variation  $\theta$  of the subsarcolemmal  $\text{Ca}^{2+}$  concentration as a function of  $\gamma$  and  $i_{\text{Ca}}$ . All other parameter values as in Table 1.

155 vanishes irrespective of the value of  $\gamma$ , indicating that synchrony is stable and does not depend on how quickly  $\text{Ca}^{2+}$ -dependent inactivation sets in. For larger values of  $i_{\text{Ca}}$ , we observe a sharp transition from synchrony (blue) to alternans (yellow) upon increase of  $\gamma$ . Hence, for a sufficiently strong unitary L-type  $\text{Ca}^{2+}$  current, subcellular  $\text{Ca}^{2+}$  alternans can be induced if  $\text{Ca}^{2+}$ -dependent inactivation becomes more switch-like. When  $\text{Ca}^{2+}$ -dependent inactivation sets in more  
 160 gradually, i.e.  $\gamma$  is small, synchrony is stable as we increase  $i_{\text{Ca}}$ . However, for

larger values of  $\gamma$ , we observe a sharp transition from synchrony to subcellular  $\text{Ca}^{2+}$  alternans as the L-type  $\text{Ca}^{2+}$  channel becomes stronger. There appears to be an L-shape stability boundary in that for a large range of  $\gamma$ , subcellular  $\text{Ca}^{2+}$  alternans appear for approximately the same value of  $i_{\text{Ca}}$ , while for a large range of  $i_{\text{Ca}}$ , alternans set in for approximately the same small value of  $\gamma$ . We also note that the transition from stable synchrony to subcellular  $\text{Ca}^{2+}$  alternans is quite abrupt, as indicated by the sharp transition from blue to yellow. Taken together, our findings provide strong evidence that the L-type  $\text{Ca}^{2+}$  channel can initiate subcellular  $\text{Ca}^{2+}$  alternans, either via its  $\text{Ca}^{2+}$ -dependent inactivation or the strength of its unitary  $\text{Ca}^{2+}$  current.

#### 4. Buffers

All results so far were obtained for constant buffer contributions. In other words, we set  $\beta(c_1^\mu)$  and  $\beta(c_s^\mu)$  to constants  $\beta_i$  and  $\beta_s$ , respectively, consistent with earlier work [11]. In this way, we eliminate any time-dependent modulation of the  $\text{Ca}^{2+}$  dynamics through binding and unbinding to  $\text{Ca}^{2+}$  buffers. Under more general conditions, however, Eq. (4) entails that  $\beta(c_1^\mu)$  and  $\beta(c_s^\mu)$  oscillate with the same frequency as  $c_1^\mu$  and  $c_s^\mu$ , respectively. Figure 6A illustrates that in this case, subcellular  $\text{Ca}^{2+}$  alternans can be abolished and synchrony is stable. This behaviour needs to be contrasted with that depicted in Fig. 4B, which we would obtain with the parameter values used in Fig. 6A upon replacing the dynamic buffers with the constant buffers used in Fig. 4B. In other words, while the dynamics of the L-type  $\text{Ca}^{2+}$  channel can induce subcellular  $\text{Ca}^{2+}$  alternans (as demonstrated in Fig. 4), dynamic  $\text{Ca}^{2+}$  buffers can rescue this pathological behaviour. This discrepancy between constant and time-dependent buffers prompted us to explore another form of non-responsive buffers. The sensitivity of buffers is usually determined by their dissociation constants, which in the present study are the three constants  $K_{\text{SR}}$ ,  $K_{\text{Cd}}$  and  $K_{\text{T}}$  in Eq. (4), as well as the corresponding concentration of binding sites  $B_{\text{SR}}$ ,  $B_{\text{Cd}}$  and  $B_{\text{T}}$ . By choosing appropriate values, we can effectively “desensitise” the  $\text{Ca}^{2+}$  buffers. As

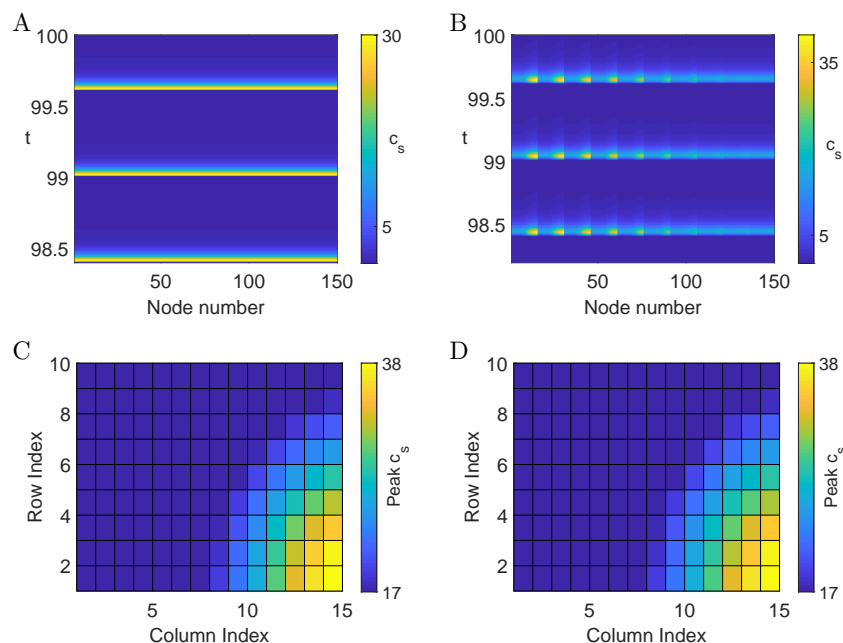


Figure 6: Space-time plot of the subarcolemmal  $\text{Ca}^{2+}$  concentration of the unravelled CRU network for (A) fully nonlinear buffers and (B) desensitised buffers (C,D) Peak subarcolemmal  $\text{Ca}^{2+}$  concentration on two successive beats across the CRU network. Parameter values as in (B). Other parameter values as in Table 1 and  $K_{\text{SR}} = 6.0\mu\text{M}$ ,  $K_{\text{T}} = 600.0\mu\text{M}$ ,  $K_{\text{Cd}} = 7.0\mu\text{M}$ ,  $B_{\text{SR}} = 250.0\mu\text{ mol/1 cytosol}$ ,  $B_{\text{T}} = 12000.0\mu\text{ mol/1 cytosol}$ ,  $B_{\text{Cd}} = 1.0\mu\text{ mol/1 cytosol}$ .

Figs. 6B–6D illustrate for the desensitised dynamics, subcellular  $\text{Ca}^{2+}$  alternans re-emerge consistent with a saddle-node bifurcation. Figure 6B shows a space-time plot of the unravelled CRU network. Each CRU follows a period-1 orbit, which differs both in amplitude and duration of the  $\text{Ca}^{2+}$  transient across the network, as can be deduced from the variation of the yellow wedges. A more detailed view on the spatial pattern is provided in Figs. 6C and 6D, which depict peak amplitudes of the subarcolemmal  $\text{Ca}^{2+}$  concentration on successive beats. Note that although the subcellular  $\text{Ca}^{2+}$  alternans emerge through a saddle-node bifurcation, the spatial pattern differs from that observed in Figs. 3 and 4. This is consistent with our earlier findings, which have demonstrated a

rich pattern space of subcellular  $\text{Ca}^{2+}$  alternans [12, 13].

At this point, one might be tempted to conclude that constant buffers make the occurrence of subcellular  $\text{Ca}^{2+}$  alternans more likely. However, as Fig. 7A reveals, this is not the case. Leaving all parameter values unchanged but setting  
 205  $\beta_s = \beta_i = 1$  we find synchrony. Crucially, these simulations correspond to the case without buffers and should be contrasted with the results in Fig. 6A. In both cases, synchrony is stable, but the reasons as to why might differ. The constant

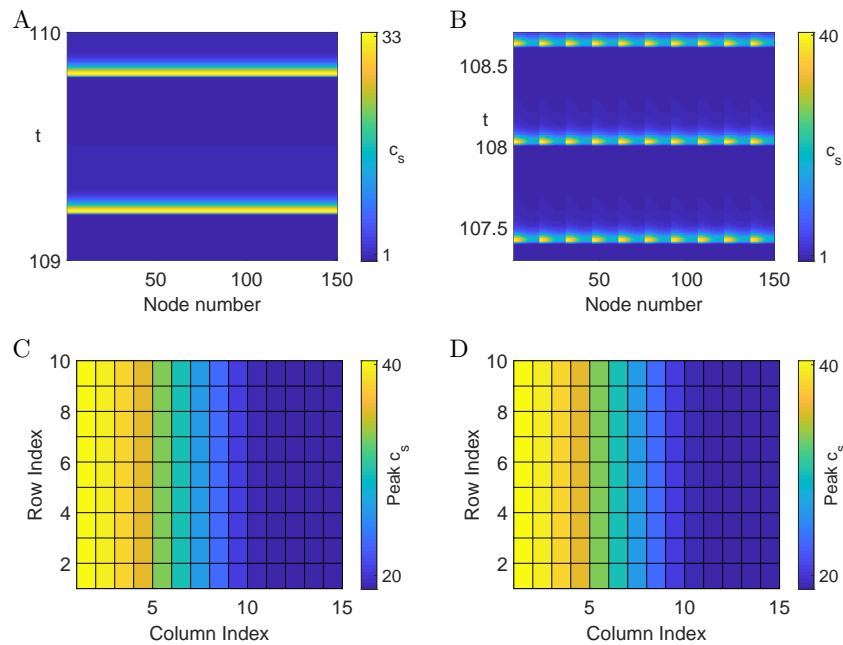


Figure 7: Space-time plot of the subsarcolemmal  $\text{Ca}^{2+}$  concentration of the unravelled CRU network for  $T_p = 0.6\text{s}$  and (A)  $\beta_s = \beta_i = 1$ , (B)  $\beta_s = 0.08827$ ,  $\beta_i = 0.01738$ . (C,D) Peak subsarcolemmal  $\text{Ca}^{2+}$  concentration on two successive beats across the CRU network. Parameter values as in (B). For all other parameter values, see Table 1.

values for  $\beta_s$  and  $\beta_i$  that we used in Sect. 3.1 were obtained for a piecewise linear (PWL) caricature of the model given by Eq. (1), see [11] for details. To obtain  
 210 estimates that are more consistent with the full nonlinear model, we determine the mean values of  $\beta(c_s^t)$  and  $\beta(c_i^t)$  when synchrony is stable and assign them

to  $\beta_s$  and  $\beta_i$ , respectively. For these values, we find subcellular  $\text{Ca}^{2+}$  alternans that are consistent with a saddle-node bifurcation as shown in Figs. 7B. Again, individual CRUs display a period-1 orbit, which differs throughout the network.  
 215 The spatial pattern of the subcellular  $\text{Ca}^{2+}$  alternans is reminiscent of the one depicted in Figs. 3B – 3D, where  $\text{Ca}^{2+}$  transients are more pronounced on the left side of the CRU network compared to the right side.

Since constant  $\text{Ca}^{2+}$  buffers can both promote as well as abolish subcellular  $\text{Ca}^{2+}$  alternans, we next explore the impact of the buffer time course on the  
 220 formation of subcellular  $\text{Ca}^{2+}$  alternans. To do this in a controlled fashion, we extract the time course of both  $\beta(c_s^t)$  and  $\beta(c_i^t)$  from the full nonlinear model and then clamp the buffer time courses at each node to these profiles. In other words, each node experiences nonlinear buffer dynamics, but the buffers do not alternate from node to node. As Fig. 8A reveals, we obtain subcellular

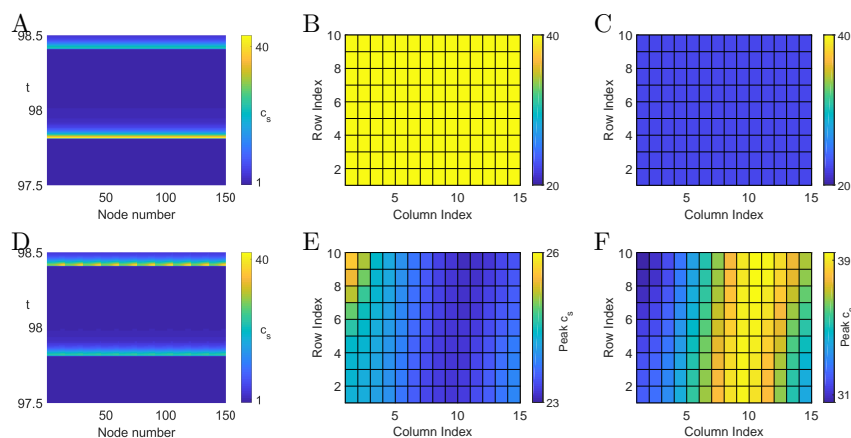


Figure 8: Network dynamics for  $T_p = 0.6\text{s}$  and clamped nonlinear buffers for (A–C)  $\sigma_{\text{sr}} = 30\text{s}^{-1}$ ,  $\sigma_c = 1\text{s}^{-1}$ , (D–F)  $\sigma_{\text{sr}} = 3\text{s}^{-1}$ ,  $\sigma_c = 0\text{s}^{-1}$ . Space-time plots of the subsarcolemmal  $\text{Ca}^{2+}$  concentration of the unravelled CRU are shown in (A) and (D). Peak subsarcolemmal  $\text{Ca}^{2+}$  concentration on two successive beats across the CRU network are plotted in (B,C) and (E,F). For all other parameter values, see Table 1.

225  $\text{Ca}^{2+}$  alternans that differ from those reported so far in this study. Here, every node in the network follows the same period-2 orbit characteristic of subcellular

$\text{Ca}^{2+}$  alternans that emerge via a period-doubling bifurcation. Figures 8B and 8C illustrate the uniform behaviour across the network that alternates between successive beats. This spatial pattern is known as spatially concordant  $\text{Ca}^{2+}$  alternans. When we change the coupling strengths, but keep all other parameter values unaltered, we observe spatially discordant  $\text{Ca}^{2+}$  alternans as plotted in Figs. 8D–8F. Every node follows a period-2 orbit, but different parts of the network oscillate out-of-phase with each other.

Our results so far strongly suggest that the time course and amplitude of  $\text{Ca}^{2+}$  buffers significantly impacts on the genesis of subcellular  $\text{Ca}^{2+}$  alternans. Figure 9 shows results from an *in silico* experiment in which we tune the  $\text{Ca}^{2+}$  buffer dynamics from constant ( $\varepsilon = 0$ ) to fully nonlinear ( $\varepsilon = 1$ ). As a measure for the strength of subcellular  $\text{Ca}^{2+}$  alternans, we report the maximal beat-to-beat variation  $\theta$  as defined after Eq. (5). As  $\varepsilon$  increases, we find a monotonic decrease in  $\theta$ , highlighting that nonlinear buffers have the potential to abolish subcellular  $\text{Ca}^{2+}$  alternans.

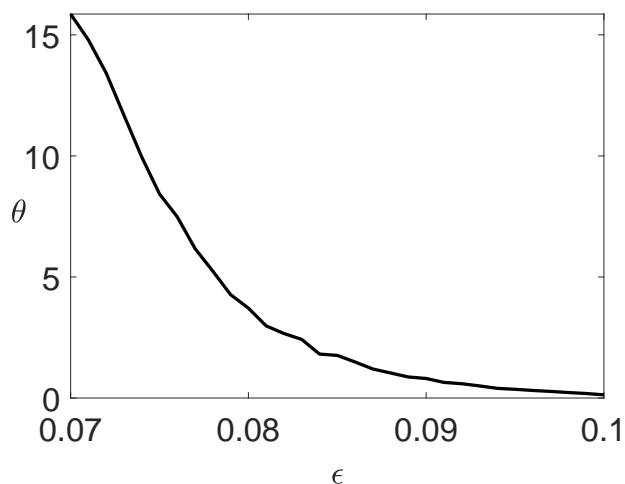


Figure 9: Maximal beat-to-beat variation  $\theta$  of the subsarcolemmal  $\text{Ca}^{2+}$  concentration as a function of the variability of the  $\text{Ca}^{2+}$  buffer  $\varepsilon$ . See text for details. Parameter values as in Table 1.



## 5. Discussion

Subcellular  $\text{Ca}^{2+}$  alternans have been firmly linked to the genesis of cardiac arrhythmias. Despite this crucial connection, we still lack a complete picture of how the dynamics of the intracellular  $\text{Ca}^{2+}$  concentration transitions from its healthy period-1 orbit to its various pathological forms.

Our focus has been on understanding subcellular  $\text{Ca}^{2+}$  alternans in tubulated myocytes, such as ventricular myocytes. The presence of t-tubules in these cells gives rise to well-defined CRUs, which form a network where nearest neighbours are coupled via  $\text{Ca}^{2+}$  diffusion, both through the cytosol and the SR. The discussion of whether  $\text{Ca}^{2+}$  diffusion in the SR is fast or slow has been ongoing for more than a decade [21–23], without a resolution in sight. We illustrate in Figs. 1 and 2 that whether  $\text{Ca}^{2+}$  diffuses more dominantly in the lumen or in the cytosol has major consequences for the spatial patterns of subcellular  $\text{Ca}^{2+}$  alternans. In the latter, subcellular  $\text{Ca}^{2+}$  alternans emerge via the classical period-doubling bifurcation, where CRUs exhibit a period-2 orbit and CRUs in different parts of the cell oscillate out-of-phase with each other. This behaviour has been well studied and documented [2–9]. On the other hand, when  $\text{Ca}^{2+}$  diffusion in the SR dominates, we observe a completely different spatial pattern originating from a saddle-node bifurcation. Here, CRUs show a period-1 orbit, which is different from the synchronous network state and where CRUs in different regions of the cell exhibit  $\text{Ca}^{2+}$  transients of varying amplitude. It is worth noting that the discussion of whether intraluminal  $\text{Ca}^{2+}$  diffusion is faster than cytosolic  $\text{Ca}^{2+}$  diffusion — a process known as intraluminal tunnelling — has already received attention, although in a different context [50]. Given the largely unexplored nature of the saddle-node bifurcation in the generation of subcellular  $\text{Ca}^{2+}$  alternans, we have concentrated on dominant luminal coupling in the present study and have investigated two main contributors that shape the dynamics of cardiac  $\text{Ca}^{2+}$ : the L-type  $\text{Ca}^{2+}$  channel and  $\text{Ca}^{2+}$  buffers.

The L-type  $\text{Ca}^{2+}$  channel constitutes a major  $\text{Ca}^{2+}$  conduit that regulates  $\text{Ca}^{2+}$  influx from the extracellular space into the myoplasm and is thus crucial

for high-fidelity excitation-contraction coupling. It is therefore not surprising that pathologies of the L-type  $\text{Ca}^{2+}$  channel can lead to abnormal  $\text{Ca}^{2+}$  dynamics. When we increase the single channel  $\text{Ca}^{2+}$  current  $i_{\text{Ca}}$ , subcellular  $\text{Ca}^{2+}$  alternans are more likely to occur as evidenced by the transition from blue to yellow in Fig. 5. However, this behaviour depends on the strength of  $\text{Ca}^{2+}$ -dependent inactivation of the L-type  $\text{Ca}^{2+}$  channel. As is often the case, the inactivation gate is modelled via a first-order kinetic scheme with a time constant  $\tau_q$  and a state-dependent steady state  $q_\infty$ . As Eq. (3) shows,  $q_\infty$  follows an inverse Hill function with exponent  $\gamma$ . Hence, for small values of  $\gamma$ ,  $q_\infty$  changes gradually as a function of the subsarcolemmal  $\text{Ca}^{2+}$  concentration  $c_s$ . On the other hand, large values of  $\gamma$  lead to a switch-like Hill function. When  $i_{\text{Ca}}$  is small, the increase in subsarcolemmal  $\text{Ca}^{2+}$  is small as well, which in turn almost completely eliminates  $\text{Ca}^{2+}$  dependent inactivation (as  $q$  never falls sufficiently towards zero). Therefore, we do not observe any effect of  $\gamma$  on the generation of subcellular  $\text{Ca}^{2+}$  alternans in this regime, indicated by the blue band towards the left of Fig. 5. On the other hand, as we increase  $i_{\text{Ca}}$ , the larger subsarcolemmal  $\text{Ca}^{2+}$  concentrations allow for a larger exploration of the right tail of  $q_\infty$ , and hence values closer to zero. When  $\gamma$  is large making  $q_\infty$  more step-like, bigger values of  $c_s^\mu$  entail longer periods where  $q$  tends to zero. An increase of  $i_{\text{Ca}}$  does not change that, meaning that the nature of the subcellular  $\text{Ca}^{2+}$  alternans is not affected by increasing  $i_{\text{Ca}}$  for larger values of  $\gamma$ . This explains the almost uniform yellow colouring in Fig. 5 for fixed large  $\gamma$  and varying  $i_{\text{Ca}}$ . An interesting feature of Fig. 5 is the sharp transition from regular behaviour to subcellular  $\text{Ca}^{2+}$  alternans as is manifest from the abrupt colour change from blue to yellow. It remains to be seen whether this behaviour can be understood more formally in terms of a phase transition.

All results for the L-type  $\text{Ca}^{2+}$  channel were obtained with constant buffer contributions. However, since the concentration of  $\text{Ca}^{2+}$  bound buffers directly depends on the intracellular  $\text{Ca}^{2+}$  concentration, the buffer function  $\beta$  in Eq. (4) should evolve over time. Using the full nonlinear buffers, we find that subcellular  $\text{Ca}^{2+}$  alternans are extinguished (Fig. 6A). In other words, solely changing the

buffer dynamics completely alters the dynamics of the cardiac cell. These findings are in line with a large body of literature demonstrating that  $\text{Ca}^{2+}$  buffers  
305 can substantially modify intracellular  $\text{Ca}^{2+}$  dynamics. From a physiological perspective, our results indicate that  $\text{Ca}^{2+}$  buffers can perform a stabilising role that can compensate for dysfunctions of other components of the  $\text{Ca}^{2+}$  signalling toolkit, such as the L-type  $\text{Ca}^{2+}$  channel. Because  $\text{Ca}^{2+}$  buffers are slaved to the  $\text{Ca}^{2+}$  dynamics, the buffer dynamics exhibit alternans as soon as the in-  
310 tracellular  $\text{Ca}^{2+}$  concentration alternates. For the results in Fig. 8, we broke this connection and clamped the  $\text{Ca}^{2+}$  buffer dynamics in such a way that each node exhibits the same nonlinear orbit. In other words,  $\text{Ca}^{2+}$  buffers alternate at each node, but there is no spatial variation of the buffer dynamics. In this regime, the patterns of the subcellular  $\text{Ca}^{2+}$  alternans vary drastically from the  
315 ones we observed so far. We found spatially concordant alternans, which can transition into spatially discordant alternans upon altering the coupling strength of cytosolic and SR diffusion. While we employed buffers to induce this pattern change, it is conceivable that such dynamics could originate from other dynamical variables of cardiac  $\text{Ca}^{2+}$  cycling. In this case, our results point to more  
320 subtle dependencies in that the nonlinear dynamics of cardiac  $\text{Ca}^{2+}$  cycling can be easily disturbed into new dynamic regimes, potentially inducing a plethora of cardiac arrhythmias. It is therefore astonishing that cardiac  $\text{Ca}^{2+}$  dynamics more often than not behaves completely regularly; a fact that certainly deserves more attention.

325 We first reported the emergence of subcellular  $\text{Ca}^{2+}$  alternans via a saddle-node bifurcation in a PWL caricature of an established  $\text{Ca}^{2+}$  cycling model [12]. One might wonder if this novel form of subcellular  $\text{Ca}^{2+}$  alternans is a consequence of the approximations used in the derivation of the PWL model. The results presented here show that this is not the case. The fully nonlinear  
330 model exhibits the same instabilities. This provides further evidence that PWL models are valuable in exploring the behaviour of complex nonlinear systems and thus adds to earlier success stories such as the McKean model, which represents a PWL version of the Fitzugh-Nagumo model for the propagation of

neural action potentials [51–53]. The advantage of PWL models is that the  
335 majority of the analysis can be performed semi-analytically, which greatly facil-  
itates the exploration of the associated parameter space. In turn, this allows for  
a more comprehensive classification of the possible dynamics. In contrast, fully  
nonlinear systems can often only be dissected via direct numerical simulations,  
which is often only done for a small subset of parameter values. In this respect,  
340 PWL models can provide guidance for the analysis of the nonlinear systems and  
where to explore in parameter space for interesting behaviour.

The last point becomes especially pertinent for the exploration of the differ-  
ent spatial patterns that emerge via a saddle-node bifurcation. As Figs. 1, 2,  
6 and 8 illustrate, the  $\text{Ca}^{2+}$  profiles across the network exhibit significant vari-  
345 ability. In a PWL model, these patterns can be classified and understood from  
a linear stability analysis, which can be performed in closed form [12, 13]. On  
the other hand, the nonlinear model requires direct simulations, which are com-  
putationally more expensive and limited in scope as to what parameter values  
to sample.

350 As stated above, our focus here is on tubulated myocytes. However,  $\text{Ca}^{2+}$   
alternans have also been observed in non-tubulated cells such as atrial myocytes  
and failing ventricular myocytes [54–60]. In these cells, L-type  $\text{Ca}^{2+}$  channels  
are only located at the cell periphery, where they trigger  $\text{Ca}^{2+}$  release from the  
SR through the RyR. A  $\text{Ca}^{2+}$  wave then propagates centripetally from the pe-  
355 riphery via diffusion and  $\text{Ca}^{2+}$  induced  $\text{Ca}^{2+}$  release [61, 62]. Conceptually, it  
therefore makes sense to distinguish junctional CRUs (that contain L-type  $\text{Ca}^{2+}$   
channels) and non-junctional CRUs (that lack L-type  $\text{Ca}^{2+}$  channels). Due to  
the stronger reliance on  $\text{Ca}^{2+}$  diffusion, it will be interesting to explore how  
differences in the diffusive coupling between CRUs and the fact there are two  
360 classes of CRUs shape subcellular  $\text{Ca}^{2+}$  alternans and whether the bifurcation  
structure observed for tubulated myocytes carries over to non-tubulated ones.  
Answering this question will not only unravel further similarities or differences  
between tubulated and non-tubulated myocytes, it will also advance our under-  
standing of atrial fibrillation, which is projected to become epidemic with an

365 ageing population [63].

## Acknowledgement

This work was supported by the Engineering and Physical Sciences Research Council [grant number EP/P007031/1].

## Appendix

370 We here provide the parameter values used in the study unless otherwise stated.

	Definition	Value
T	Temperature	308 K
F	Faraday's constant	96.4867 C/mmol
R	Gas constant	8.314 J/K mol
$\text{Na}_o$	External sodium concentration	140 mM
$\text{Ca}_o$	External calcium concentration	1.8 mM
$v_s/v_i$	Subsarcolemmal/cell volume	0.1
$c_{\text{up}}$	Uptake threshold	0.5 $\mu\text{M}$
$v_{\text{up}}$	Uptake strength	270 $\mu\text{M/s}$
$\bar{I}_{\text{NaCa}}$	Strength of the NaCa exchanger	$10^5 \mu\text{M/s}$
$k_{\text{sat}}$	Constant from the 1994 Luo-Rudy model	0.1
$\xi$	Constant from the 1994 Luo-Rudy model	0.35
$K_{\text{mNa}}$	Constant from the 1994 Luo-Rudy model	87.5 mM
$K_{\text{mCa}}$	Constant from the 1994 Luo-Rudy model	1.38 mM
$\gamma_s$	Constant from the 1994 Luo-Rudy model	1
$\gamma_o$	Constant from the 1994 Luo-Rudy model	0.341
$P_{\text{Ca}}$	Constant from the 1994 Luo-Rudy model	$5.4 \times 10^{-4} \text{ cm/s}$
$i_{\text{Ca}}$	Flux constant	6600 $\mu \text{ mol/C cm}$
$\tau_{\text{f}}$	Time constant for voltage-dependent inactivation	30 ms
$\tau_{\text{d}}$	Time constant for voltage-dependent activation	5ms

$\tau_q$	Time constant for $\text{Ca}^{2+}$ -dependent inactivation	20 ms
$\tilde{c}_c$	Calcium inactivation threshold	$0.5 \mu\text{M}$
$\gamma$	Sensitivity parameter for calcium dependent inactivation	4
$g$	Release current strength	$3.5 \times 10^4 \text{ sparks}/\mu\text{M}$
$u$	Release slope	$11.3 \text{ s}^{-1}$
$\tau_r$	Average spark life time	20 ms
$\tau_a$	Relaxation time of $c_u$ to $c_j$	50 ms
$\tau_s$	Submembrane diffusion time constant	10 ms
$B_T$	Total concentration of troponin C binding sites	$70 \mu\text{mol}/1 \text{ cytosol}$
$B_{\text{SR}}$	Total concentration of SR binding sites	$47 \mu\text{mol}/1 \text{ cytosol}$
$B_{\text{Cd}}$	Total concentration of calmodulin binding sites	$24 \mu\text{mol}/1 \text{ cytosol}$
$K_T$	Dissociation constant for troponin C binding sites	$0.6 \mu\text{M}$
$K_{\text{SR}}$	Dissociation constant for SR binding sites	$0.6 \mu\text{M}$
$K_{\text{Cd}}$	Dissociation constant for calmodulin binding sites	$7 \mu\text{M}$
$\beta_s$	Buffering constant for $c_s$	0.5
$\beta_i$	Buffering constant for $c_i$	0.01
$\sigma_c$	Coupling strength in cytosol	$1 \text{ s}^{-1}$
$\sigma_c$	Coupling strength in the SR	$30 \text{ s}^{-1}$

Table 1: Standard parameter values used in the study.

## References

- [1] Adabag, A.S., Luepker, R.V., Roger, V.L., Gersh, B.J.. Sudden cardiac death: Epidemiology and risk factors. *Nature Reviews Cardiology* 2010;7(4):216–225.
- [2] Shiferaw, Y., Karma, A.. Turing instability mediated by voltage and calcium diffusion in paced cardiac cells. *Proceedings of the National Academy of Sciences of the United States of America* 2006;103(15):5670–5675.
- [3] Rovetti, R., Cui, X., Garfinkel, A., Weiss, J.N., Qu, Z.. Spark-

- 380 induced sparks as a mechanism of intracellular calcium alternans in cardiac  
myocytes. *Circulation Research* 2010;106(10):1582–1591.
- [4] Qu, Z., Nivala, M., Weiss, J.N.. Calcium alternans in cardiac myocytes: order from disorder. *Journal of Molecular and Cellular Cardiology* 2013;58:100–109.
- 385 [5] Gaeta, S.A., Bub, G., Abbott, G.W., Christini, D.J.. Dynamical mechanism for subcellular alternans in cardiac myocytes. *Circulation Research* 2009;105(4):335–342.
- [6] Gaeta, S.A., Krogh-Madsen, T., Christini, D.J.. Feedback-control induced pattern formation in cardiac myocytes: a mathematical modeling  
390 study. *Journal of Theoretical Biology* 2010;266(3):408–418.
- [7] Gaeta, S.A., Christini, D.J.. Non-Linear dynamics of cardiac alternans: subcellular to tissue-level mechanisms of arrhythmia. *Frontiers in Physiology* 2012;3:157.
- [8] Restrepo, J.G., Karma, A.. Spatiotemporal intracellular calcium dynamics  
395 during cardiac alternans. *Chaos* 2009;19(3):037115.
- [9] Aistrup, G.L., Shiferaw, Y., Kapur, S., Kadish, A.H., Wasserstrom, J.A.. Mechanisms underlying the formation and dynamics of subcellular calcium alternans in the intact rat heart. *Circulation Research* 2009;104(5):639–649.
- [10] Tian, Q., Kaestner, L., Lipp, P.. Noise-free visualization of microscopic calcium signaling by pixel-wise fitting. *Circulation Research*  
400 2012;111(1):17–27.
- [11] Thul, R., Coombes, S.. Understanding cardiac alternans: a piecewise linear modeling framework. *Chaos* 2010;20(4):045102.
- [12] Veasy, J., Lai, Y.M., Coombes, S., Thul, R.. Complex patterns of  
405 subcellular cardiac alternans. under review 2019;.

- [13] Lai, Y.M., Veasy, J., Coombes, S., Thul, R.. A master stability function approach to cardiac alternans. under review 2019;.
- [14] Alvarez-Lacalle, E., Cantalapiedra, I.R., Peñaranda, A., Cinca, J., Hove-Madsen, L., Echebarria, B.. Dependency of calcium alternans on ryanodine receptor refractoriness. PloS One 2013;8(2):e55042–.
- [15] Tomek, J., Tomková, M., Zhou, X., Bub, G., Rodriguez, B.. Modulation of Cardiac Alternans by Altered Sarcoplasmic Reticulum Calcium Release: A Simulation Study. Frontiers in Physiology 2018;9:1306.
- [16] Huertas, M.A., Smith, G.D., Gyorke, S..  $\text{Ca}^{2+}$  Alternans in a cardiac myocyte model that uses moment equations to represent heterogeneous junctional SR  $\text{Ca}^{2+}$ . Biophysical Journal 2010;99(2):377–387.
- [17] Nivala, M., Qu, Z.. Calcium alternans in a couplon network model of ventricular myocytes: role of sarcoplasmic reticulum load. American Journal of Physiology Heart and Circulatory Physiology 2012;303(3):H341–52.
- [18] Qu, Z., Liu, M.B., Nivala, M.. A unified theory of calcium alternans in ventricular myocytes. Scientific Reports 2016;6:35625.
- [19] Díaz, M.E., O’Neill, S.C., Eisner, D.A.. Sarcoplasmic reticulum calcium content fluctuation is the key to cardiac alternans. Circulation Research 2004;94(5):650–656.
- [20] Li, Y., Díaz, M.E., Eisner, D.A., O’Neill, S.. The effects of membrane potential, SR  $\text{Ca}^{2+}$  content and RyR responsiveness on systolic  $\text{Ca}^{2+}$  alternans in rat ventricular myocytes. The Journal of Physiology 2009;587(Pt 6):1283–1292.
- [21] Swietach, P., Spitzer, K.W., Vaughan-Jones, R.D..  $\text{Ca}^{2+}$ -mobility in the sarcoplasmic reticulum of ventricular myocytes is low. Biophysical Journal 2008;95(3):1412–1427.



- [22] Picht, E., Zima, A.V., Shannon, T.R., Duncan, A.M., Blatter, L.A., Bers, D.M.. Dynamic calcium movement inside cardiac sarcoplasmic reticulum during release. *Circulation Research* 2011;108(7):847–856.
- 435 [23] Bers, D.M., Shannon, T.R.. Calcium movements inside the sarcoplasmic reticulum of cardiac myocytes. *Journal of Molecular and Cellular Cardiology* 2013;58(1):59–66.
- [24] Bers, D.M.. Cardiac excitation-contraction coupling. *Nature* 2002;415(6868):198–205.
- 440 [25] Faber, G.M., Silva, J., Livshitz, L., Rudy, Y.. Kinetic properties of the cardiac L-type  $\text{Ca}^{2+}$  channel and its role in myocyte electrophysiology: a theoretical investigation. *Biophysical Journal* 2007;92(5):1522–1543.
- [26] Shaw, R.M., Colecraft, H.M.. L-type calcium channel targeting and local signalling in cardiac myocytes. *Cardiovascular Research* 2013;98(2):177–  
445 186.
- [27] Edwards, J.N., Blatter, L.A.. Cardiac alternans and intracellular calcium cycling. *Clinical and Experimental Pharmacology & Physiology* 2014;41(7):524–532.
- [28] Mahajan, A., Sato, D., Shiferaw, Y., Baher, A., Xie, L.H., Peralta, R.,  
450 et al. Modifying L-type calcium current kinetics: consequences for cardiac excitation and arrhythmia dynamics. *Biophysical Journal* 2008;94(2):411–423.
- [29] Sato, D., Dixon, R.E., Santana, L.F., Navedo, M.F.. A model for cooperative gating of L-type  $\text{Ca}^{2+}$  channels and its effects on cardiac alternans  
455 dynamics. *PLoS Computational Biology* 2018;14(1):e1005906.
- [30] Shiferaw, Y., Watanabe, M.A., Garfinkel, A., Weiss, J.N., Karma, A.. Model of intracellular calcium cycling in ventricular myocytes. *Biophysical Journal* 2003;85(6):3666–3686.

- [31] Josephson, I.R., Guia, A., Lakatta, E.G., Lederer, W.J., Stern, M.D..  
460 Ca<sup>2+</sup>-dependent components of inactivation of unitary cardiac L-type Ca<sup>2+</sup>  
channels. *The Journal of Physiology* 2010;588(Pt 1):213–223.
- [32] Grandi, E., Morotti, S., Ginsburg, K.S., Severi, S., Bers, D.M.. Interplay  
of voltage and Ca-dependent inactivation of L-type Ca current. *Progress  
in Biophysics and Molecular Biology* 2010;103(1):44–50.
- 465 [33] Alvarez-Lacalle, E., x00F1, A.P., aranda, , Cantalapiedra, I.R., Hove-  
Madsen, L., Echebarria, B.. Effect of RyR2 refractoriness and hypercal-  
cemia on calcium overload, spontaneous release, and calcium alternans. In:  
*Computing in Cardiology* 2013. IEEE; 2013, p. 683–686.
- [34] Hake, J., Edwards, A.G., Yu, Z., Kekenés-Huskey, P.M., Michailova,  
470 A.P., McCammon, J.A., et al. Modelling cardiac calcium sparks in a three-  
dimensional reconstruction of a calcium release unit. *Journal of Physiology-  
London* 2012;590(Pt 18):4403–4422.
- [35] Kornyejev, D., Petrosky, A.D., Zepeda, B., Ferreira, M., Knollmann,  
B., Escobar, A.L.. Calsequestrin 2 deletion shortens the refractoriness of  
475 Ca<sup>2+</sup> release and reduces rate-dependent Ca<sup>2+</sup>-alternans in intact mouse  
hearts. *Journal of Molecular and Cellular Cardiology* 2012;52(1):21–31.
- [36] Stevens, S.C.W., Terentyev, D., Kalyanasundaram, A., Periasamy, M.,  
Gyorke, S.. Intra-sarcoplasmic reticulum Ca<sup>2+</sup> oscillations are driven  
by dynamic regulation of ryanodine receptor function by luminal Ca<sup>2+</sup> in  
480 cardiomyocytes. *The Journal of Physiology* 2009;587(Pt 20):4863–4872.
- [37] Restrepo, J.G., Weiss, J.N., Karma, A.. Calsequestrin-Mediated Mech-  
anism for Cellular Calcium Transient Alternans. *Biophysical Journal*  
2008;95(8):23–23.
- [38] Lee, Y.S.Y., Keener, J.P.J.. A calcium-induced calcium release mechanism  
485 mediated by calsequestrin. *Journal of Theoretical Biology* 2008;253(4):12–  
12.

- [39] Terentyev, D., Kubalova, Z., Valle, G., Nori, A., Vedamoorthyrao, S., Terentyeva, R., et al. Modulation of SR Ca release by luminal Ca and calsequestrin in cardiac myocytes: effects of CASQ2 mutations linked to sudden cardiac death. *Biophysical Journal* 2008;95(4):2037–2048.
- 490
- [40] Gyorke, S., Terentyev, D.. Modulation of ryanodine receptor by luminal calcium and accessory proteins in health and cardiac disease. *Cardiovascular Research* 2008;77(2):245–255.
- [41] Shannon, T.R.. Linking calsequestrin to lumenal control of SR  $Ca^{2+}$  release. *Circulation Research* 2007;101(6):539–541.
- 495
- [42] Beard, N.A.N., Laver, D.R.D., Dulhunty, A.F.A.. Calsequestrin and the calcium release channel of skeletal and cardiac muscle. *Progress in Biophysics and Molecular Biology* 2004;85(1):37–37.
- [43] Terentyev, D., Viatchenko-Karpinski, S., Györke, I., Volpe, P., Williams, S.C., Györke, S.. Calsequestrin determines the functional size and stability of cardiac intracellular calcium stores: Mechanism for hereditary arrhythmia. *Proceedings of the National Academy of Sciences of the United States of America* 2003;100(20):11759–11764.
- 500
- [44] Wakili, R., Yeh, Y.H., Yan Qi, X., Greiser, M., Chartier, D., Nishida, K., et al. Multiple potential molecular contributors to atrial hypocontractility caused by atrial tachycardia remodeling in dogs. *Circulation Arrhythmia and Electrophysiology* 2010;3(5):530–541.
- 505
- [45] Dobrev, D., Wehrens, X.H.T.. Calmodulin kinase II, sarcoplasmic reticulum  $Ca^{2+}$  leak, and atrial fibrillation. *Trends in Cardiovascular Medicine* 2010;20(1):30–34.
- 510
- [46] Yeh, Y.H., Wakili, R., Qi, X.Y., Chartier, D., Boknik, P., Kääh, S., et al. Calcium-handling abnormalities underlying atrial arrhythmogenesis and contractile dysfunction in dogs with congestive heart failure. *Circulation Arrhythmia and Electrophysiology* 2008;1(2):93–102.

- 515 [47] Zalk, R., Lehnart, S.E., Marks, A.R.. Modulation of the ryanodine receptor and intracellular calcium. *Annual Review of Biochemistry* 2007;76:367–385.
- [48] Smith, G.D., Wagner, J., Keizer, J.. Validity of the rapid buffering approximation near a point source of calcium ions. *Biophysical Journal* 1996;70(6):2527–2539.
- 520 [49] Wagner, J., Keizer, J.. Effects of Rapid Buffers on  $\text{Ca}^{2+}$  Diffusion and  $\text{Ca}^{2+}$  Oscillations. *Biophysical Journal* 1994;67(1):447–456.
- [50] Petersen, O.H., Courjaret, R., Machaca, K..  $\text{Ca}^{2+}$  tunnelling through the ER lumen as a mechanism for delivering  $\text{Ca}^{2+}$  entering via store-operated  $\text{Ca}^{2+}$  channels to specific target sites. *The Journal of Physiology* 2017;595(10):2999–3014.
- 525 [51] McKean, H.P.. Nagumo’s equation. *Advances in Mathematics* 1970;4(3):209–223.
- [52] FitzHugh, R.. Impulses and physiological states in theoretical models of nerve membrane. *Biophysical Journal* 1961;1(6):445–466.
- 530 [53] Nagumo, J., Arimoto, S., Yoshizawa, S.. An Active Pulse Transmission Line Simulating Nerve Axon. In: *Proceedings of the IRE*; vol. 50. 1962, p. 2061 – 2070.
- [54] Song, Z., Liu, M.B., Qu, Z.. Transverse tubular network structures in the genesis of intracellular calcium alternans and triggered activity in cardiac cells. *Journal of Molecular and Cellular Cardiology* 2017;114:288–299.
- 535 [55] Nivala, M., Song, Z., Weiss, J.N., Qu, Z.. T-tubule disruption promotes calcium alternans in failing ventricular myocytes: mechanistic insights from computational modeling. *Journal of Molecular and Cellular Cardiology* 2015;79:32–41.
- 540

- [56] Chang, K.C., Bayer, J.D., Trayanova, N.A.. Disrupted calcium release as a mechanism for atrial alternans associated with human atrial fibrillation. *PLoS Computational Biology* 2014;10(12):e1004011.
- [57] Kanaporis, G., Blatter, L.A.. Alternans in atria: Mechanisms and clinical  
545 relevance. *Medicina (Kaunas, Lithuania)* 2017;53(3):139–149.
- [58] Lugo, C.A., Cantalapiedra, I.R., Peñaranda, A., Hove-Madsen, L., Echebarria, B.. Are SR Ca content fluctuations or SR refractoriness the key to atrial cardiac alternans?: insights from a human atrial model. *American Journal of Physiology Heart and Circulatory Physiology* 2014;.
- [59] Florea, S.M., Blatter, L.A.. Regulation of cardiac alternans by  $\beta$ -  
550 adrenergic signaling pathways. *American Journal of Physiology Heart and Circulatory Physiology* 2012;.
- [60] Shkryl, V.M., Maxwell, J.T., Domeier, T.L., Blatter, L.A.. Refractoriness of sarcoplasmic reticulum  $\text{Ca}^{2+}$  release determines  $\text{Ca}^{2+}$  alternans in  
555 atrial myocytes. *American Journal of Physiology Heart and Circulatory Physiology* 2012;302(11):H2310–20.
- [61] Thul, R., Coombes, S., Roderick, H.L., Bootman, M.D.. Subcellular calcium dynamics in a whole-cell model of an atrial myocyte. *Proceedings of the National Academy of Sciences of the United States of America*  
560 2012;109(6):2150–2155.
- [62] Bootman, M.D., Smyrniak, I., Thul, R., Coombes, S., Roderick, H.L.. Atrial cardiomyocyte calcium signalling. *Biochimica et Biophysica Acta* 2011;1813(5):922–934.
- [63] Morillo, C.A., Banerjee, A., Perel, P., Wood, D., Jouven, X..  
565 Atrial fibrillation: The current epidemic. *Journal of Geriatric Cardiology* 2017;14(3):195–203.